






Formation of antihydrogen molecular ions by associative ionization

Josiah Taylor, Brandon Vargo , Daniel Hoffman , T. J. Price ,* and Robert C. Forrey [†]
 Department of Physics, Penn State University, Berks Campus, Reading, Pennsylvania 19610-6009, USA

 (Received 25 March 2024; accepted 24 April 2024; published 15 May 2024)

Recent calculations have suggested that it may be feasible to produce antihydrogen molecular ions in the near future [Zammit *et al.*, *Phys. Rev. A* **100**, 042709 (2019)]. The proposed scheme would laser excite cold antihydrogen $\bar{\text{H}}(1s)$ atoms held in a magnetic-field minimum trap and the resulting metastable $\bar{\text{H}}(2s)$ atoms would interact to form the antihydrogen molecular ion, $\bar{\text{H}}_2^-$, by associative ionization. Estimates for the efficiencies of the proposed formation and depletion processes relied on low-energy extrapolations of rate coefficients that were computed at thermal energies. In the present work, we provide quantum calculations of the rate coefficients for associative ionization and for the competing Penning ionization process, which would deplete the population of trapped $\bar{\text{H}}$. In contrast to the low-energy extrapolations, it is found that Penning ionization is the dominant ionization process at all temperatures and the relative efficiency of associative ionization is within a factor of 3 at the low temperatures required by the experimental scheme. Rate constants for single and double excitation transfer are computed as possible loss mechanisms and all rates are found to be small compared to spin-flip decay rates from Stark-induced mixing with $\bar{\text{H}}(2p)$ states.

DOI: [10.1103/PhysRevA.109.052816](https://doi.org/10.1103/PhysRevA.109.052816)

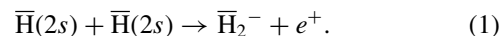
I. INTRODUCTION

One of the motivations for undertaking experiments with antimatter systems is the possibility to test the *CPT* theorem of particle physics [1–5]. Invariance with respect to charge conjugation, parity inversion, and time reversal requires that fundamental particles and their antimatter conjugates must have identical properties apart from the reversal of some quantum numbers. Violation of the *CPT* theorem would have profound implications for physics and perhaps be responsible for the lack of antiparticles in the Universe [6]. The antihydrogen molecular ion $\bar{\text{H}}_2^-$ has been identified [7,8] as a particularly desirable candidate for experimental study due to its increased sensitivity to *CPT* tests compared to the atomic case.

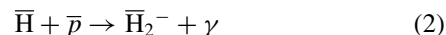
Based on combined antiparticle and antiatom traps, with their long lifetimes for all confined species [2,9,10], and the important role played by H_2^+ in the chemistry of the early Universe [11,12], the formation of $\bar{\text{H}}_2^-$ was further identified [13] as a key gateway to produce more complex antimatter species, including neutral molecular antihydrogen and charged clusters.

Laser cooling of antihydrogen atoms and application to $1S$ - $2S$ spectroscopy [10,14] provides a transformative tool for antimatter studies, including the possibility to create antimatter molecules. In a previous study [13], several mechanisms for producing $\bar{\text{H}}_2^-$ were investigated and an experimental scheme was proposed that relied on antihydrogen atoms, $\bar{\text{H}}$, held in a magnetic-field minimum trap. Laser driven

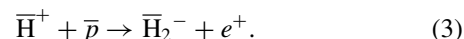
production of metastable $\bar{\text{H}}(2s)$ atoms via two-photon transitions would provide the reactants and the desired antihydrogen molecular ion would form with the emission of a positron (e^+) through the process of associative ionization (AI)



This process is the antimatter analog for the formation of H_2^+ from a pair of $\text{H}(2s)$ atoms. The $\bar{\text{H}}_2^-$ molecule may also be formed by radiative association (RA)

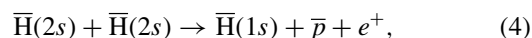


and by associative detachment (AD)



Reference [13] estimated there would not be a sufficient number density of antiprotons (\bar{p}) in the trap for RA to be a competitive process and argued the requirement of an intermediate $\bar{\text{H}}^+$ ion would render the AD process to be impractical [15]. Therefore, the study concluded that the AI process (1) for a spin-polarized gas would be the most promising approach to forming $\bar{\text{H}}_2^-$. AI with other states of $\bar{\text{H}}$ has been suggested as a possible pathway [16]; however, this is not considered here.

The metastable $\bar{\text{H}}(2s)$ atoms have a natural lifetime of ~ 120 ms [17] but may be depleted by Stark-induced mixing with $\bar{\text{H}}(2p)$ states due to the $\vec{v} \times \vec{B}$ induced field. The single-photon decay to $\bar{\text{H}}(1s)$ can flip the positron spin to an untrappable hyperfine state [17] and has been estimated to be the largest source of trap loss for the proposed scheme [13]. The $\bar{\text{H}}$ atoms may also be depleted by Penning ionization (PI)



*Current address: Alvernia University, 400 Saint Bernardine St, Reading, Pennsylvania 19607, USA.

[†]Corresponding author: rcf6@psu.edu

by double excitation transfer (DET)

$$\bar{\text{H}}(2s) + \bar{\text{H}}(2s) \rightarrow \bar{\text{H}}(2p) + \bar{\text{H}}(2p), \quad (5)$$

and by single excitation transfer (SET)

$$\bar{\text{H}}(2s) + \bar{\text{H}}(2s) \rightarrow \bar{\text{H}}(2s) + \bar{\text{H}}(2p), \quad (6)$$

which adds to the spin-flip loss. It is assumed that hot positrons produced by ionization would exit the trap without disrupting any of the cold antihydrogen species. The previous study [13] proposed lowering temperature and the magnetic-field strength of the trap to mitigate Stark-induced losses. In order to utilize a weak magnetic trapping field, a substantial fraction of the antihydrogen atoms would need to be laser-cooled into the mK regime [14,18], and the magnetic field would need to be lowered as much as possible before turning on the 1s-2s laser to drive the AI process (1). Formation rates were estimated to be around 10^{-2} s^{-1} for an $\bar{\text{H}}(2s)$ density of 10^3 cm^{-3} at a temperature of 1 mK. While this formation rate for $\bar{\text{H}}_2^-$ is rather low, there was cautious optimism [13] that the proposed scheme may be achievable as further gains in $\bar{\text{H}}$ trapping and cooling capabilities improve. The present study aims to provide reliable theoretical data to help guide this effort. We used antimatter notation above to emphasize the motivation for the present work, but the more familiar hydrogen notation is used below when describing potential-energy curves. As in the previous study, we assume in the present work that the magnetic field is sufficiently weak that its effect on the scattering processes is negligible.

High-energy fitting formulas [19] were used to estimate the relative contribution of AI and PI at the low energies required by the proposed scheme [13]. These formulas are based on quantum calculations that used a degenerate internal states ($2s$ and $2p$) approximation which neglects coupling from fine structure and Lamb shift. This yielded respective cross sections for AI and PI that behave as E^{-1} and $E^{-2/3}$ for energies greater than 10^{-4} eV . The coefficient for the PI cross section is much larger than for the AI cross section, so PI is the dominant ionization process at thermal energies. However, extrapolation of the fitting formulas leads to a crossing at $E \approx 10^{-7} \text{ eV}$ and it was estimated [13] that AI would dominate at lower energies. In the present work, we find there is no such crossing when the degenerate states approximation is used at lower energies. Furthermore, the AI and PI cross sections are substantially reduced when the atomic fine-structure and Lamb shift couplings are included in the calculation. This was taken into consideration in [13] by rescaling the AI and PI contributions obtained from the high-energy formulas to total ionization cross sections that were available from a separate set of low-energy calculations [20]. The low-energy calculations neglected nonadiabatic radial couplings that were later found to be important [21] and used a complex optical potential to compute the total ionization cross section, so the relative AI and PI contributions were not resolved. In order to resolve these contributions and provide better estimates of the rate coefficients required to simulate the proposed scheme to produce $\bar{\text{H}}_2^-$ molecules [13], we investigate the AI formation process (1) and the competing depletion processes (4)–(6) in a quantum formulation that includes all electronic states that couple to the entrance channel comprised of pairs of spin-polarized $\bar{\text{H}}(2s)$ atoms.

The previous set of low-energy calculations [20] should be replaced by the new set of improved calculations which includes the nonadiabatic radial coupling that modifies the DET cross sections at low energy and is responsible for the SET process at all energies [21]. The importance of nonadiabatic angular coupling is analyzed and the recommended rate coefficients are provided for a large range of temperatures.

II. THEORY

Following previous work [21], scattering and ionization are studied using a close-coupling expansion of the form

$$\Psi(\vec{r}_1, \vec{r}_2; \vec{R}) = \frac{1}{R} \sum_n \phi_n(\vec{r}_1, \vec{r}_2; \vec{R}) u_n(\vec{R}), \quad (7)$$

where \vec{r}_1 and \vec{r}_2 are the position vectors of the electrons with respect to the center of mass of the nuclei and $\{\phi_n\}$ is an orthonormal basis set of products of atomic functions. A noninertial body-fixed coordinate system may be used which rotates the z axis so that it is always pointing along the direction of internuclear separation \vec{R} . This simplifies the potential energy but introduces kinetic Coriolis couplings that fall off slowly at large R . Alternatively, a space-fixed coordinate system may be used which utilizes a gauge transformation [22] to remove all nonadiabatic angular couplings that may occur in the separated atom limit; however, this transformation was found to introduce complications in the molecular region for the present system [21]. Since ionization occurs at short distances, we use a coupled states (CS) formulation which neglects the nonadiabatic angular coupling arising from the Coriolis interaction. The electronic Hamiltonian may be written as

$$H_{\text{el}}(\vec{r}_1, \vec{r}_2; R) = \sum_n |\xi_n(\vec{r}_1, \vec{r}_2; R)\rangle V_n(R) \langle \xi_n(\vec{r}_1, \vec{r}_2; R)|, \quad (8)$$

where $\xi_n(\vec{r}_1, \vec{r}_2; R)$ is a molecular eigenfunction with complex eigenvalue $V_n(R) = E_n - \frac{i}{2}\Gamma_n$. The Born-Oppenheimer energies $\{E_n\}$ and autoionization widths $\{\Gamma_n\}$ have been computed previously [23,24]. Adiabatic potential-energy curves included in the calculation are shown in panel (a) of Fig. 1. The autoionization widths for the $^3\Sigma_u^+$ states are close to zero for $R > 15a_0$. The widths for the other H_2 states are neglected; the error introduced by doing so is expected to be negligible [21].

The atomic basis set in (7) may be defined by the quantum numbers $\{l_a, m_a, l_b, m_b, S, \Sigma\}$, where l_a, m_a and l_b, m_b are the electronic orbital angular momentum and projection quantum numbers for atoms a and b , and S and Σ are the total electronic spin angular momentum and projection quantum numbers. For cold collisions, the atomic fine-structure and Lamb shift energy splittings are important and it is convenient to transform the atomic basis set to the total angular momentum representation where these interactions are diagonal. The transformed basis set $\{\psi_n\}$ may be defined by the quantum numbers $\{l_a, l_b, j_a, j_b, j, \Omega\}$, where $\vec{j}_a = \vec{l}_a + \vec{s}_a$, $\vec{j}_b = \vec{l}_b + \vec{s}_b$, and $\vec{j} = \vec{j}_a + \vec{j}_b$ is the total internal angular momentum with projection Ω along the space-fixed z axis. Basis sets that are

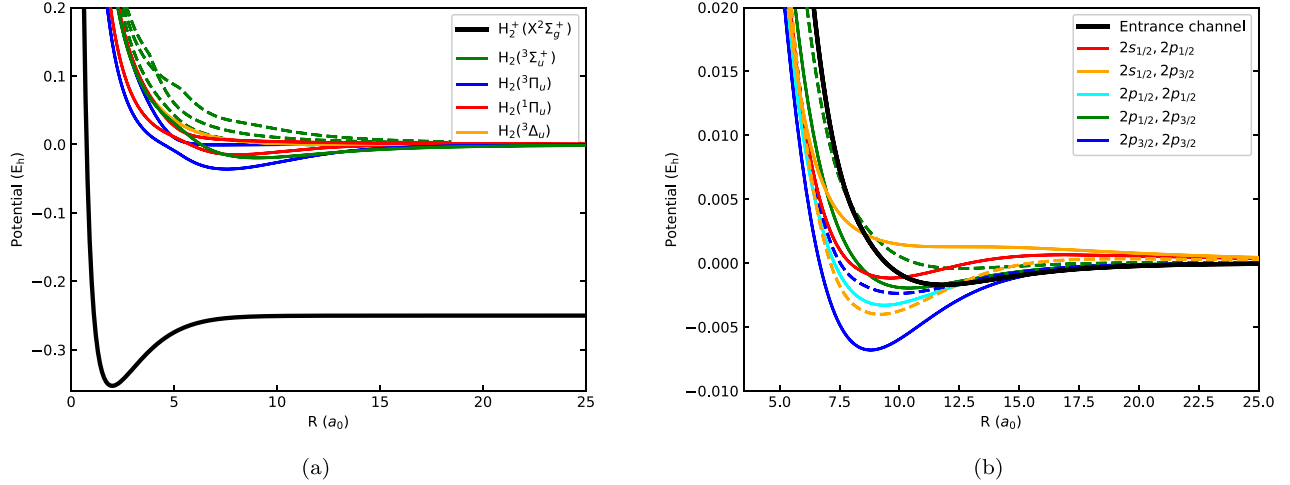


FIG. 1. Panel (a) shows the Born-Oppenheimer (adiabatic) potential-energy curves for H_2^+ and H_2 involved in the calculation. The entrance channel is the $^3\Sigma_u^+$ state of H_2 shown as a solid green curve. The dashed green curves are the other $^3\Sigma_u^+$ states that are not the entrance channel. Panel (b) shows the diagonal elements of the coupling matrix $\tilde{V}_{nm'}$ used in the coupled set of equations of Eq. (16). The legend partly specifies the asymptotic limit of each curve; parity and spin are omitted for the sake of clarity. A full specification is in Ref. [21]. Data for the H_2 and H_2^+ curves are from [24] and [25], respectively.

symmetric with respect to inversion of the nuclei may be defined as

$$|\phi\rangle = \frac{|l_a, m_a, l_b, m_b\rangle + \rho_\phi |l_b, m_b, l_a, m_a\rangle}{\sqrt{2(1 + \delta_{l_a, l_b} \delta_{m_a, m_b})}} |S, \Sigma\rangle, \quad (9)$$

$$|\psi\rangle = \frac{|l_a, l_b, j_a, j_b\rangle + \rho_\psi |l_b, l_a, j_b, j_a\rangle}{\sqrt{2(1 + \delta_{l_a, l_b} \delta_{j_a, j_b})}} |j, \Omega\rangle, \quad (10)$$

where $\rho_\phi = p\sigma(-1)^{l_a+l_b}$ and $\rho_\psi = p(-1)^{l_a+l_b+j+j_b-j_a}$, with $p = +1/-1$ for gerade (ungerade) symmetry and $\sigma = +1/-1$ for $S = 0/1$. The atomic states (9) and (10) are also symmetrized with respect to electron exchange when computing overlaps with molecular states. This yields the diabatic potential

$$V_{ij}(R) = \sum_k U_{ik}(R) V_k(R) U_{kj}^T(R), \quad (11)$$

where

$$U_{ij}(R) \equiv \sum_k \langle \psi_i(\vec{r}_1, \vec{r}_2; R) | \phi_k(\vec{r}_1, \vec{r}_2; R) \rangle \times \langle \phi_k(\vec{r}_1, \vec{r}_2; R) | \xi_j(\vec{r}_1, \vec{r}_2; R) \rangle \quad (12)$$

is a unitary matrix when the atomic basis set $\{\phi_n\}$ is complete. The R dependence of U_{ij} is needed to account for nonadiabatic radial coupling between the $(2s, 2p)$ and $(2p, 2p)$ states arising from the electrostatic dipole-quadrupole interaction [24].

For practical calculations, we restrict the basis set to include 64 atomic states corresponding to $n_1 = n_2 = 2$. The ungerade symmetry of the spin-polarized entrance channel reduces the number of basis functions to the 36 states reported previously [21] and neglecting Coriolis coupling further reduces the number of basis states to 9, each with $\Omega = 1$. Restricting the basis set to include atomic states with $n = 2$ provides negligible basis set truncation error for $R > 20$ a.u. At shorter distances, the truncated atomic basis set leads to a numerical loss of unitarity [24] for the transformation to the adiabatic molecular basis, given by Eq. (12). Delta function normalization of the diabatic basis set may be enforced by

inverting the overlap matrix

$$g_{ij} = \sum_k U_{ik}(R) U_{kj}^T(R) \quad (13)$$

to obtain reciprocal basis functions

$$\tilde{\psi}_i = \sum_j g_{ij}^{-1} \psi_j \quad (14)$$

with $\langle \tilde{\psi}_i | \psi_j \rangle = \delta_{ij}$. Matrix elements between $\tilde{\psi}_i$ and ψ_j yield the modified potential

$$\tilde{V}_{ij}(R) = \sum_k g_{ik}^{-1} V_{kj}, \quad (15)$$

which is asymmetric at short distances. This procedure does not eliminate basis set truncation error; however, it enables it to be more easily analyzed and controlled. Figure 1(b) shows the diagonal elements of the matrix $\tilde{V}_{nm'}$. For the entrance channel, there is a repulsive wall around 7.5 a.u. which shields the system from entering the region where errors in the off-diagonal elements are most severe. The centrifugal barrier also helps to shield higher partial waves from entering the small- R region. The sensitivity of the numerical results to the basis set truncation error is studied below and found to be negligible.

If the R dependence of the overlap matrix (13) is slowly varying, the radial derivative coupling may be neglected, and we may generalize the single channel approach [19] to obtain a set of inhomogeneous differential equations

$$\left[-\frac{1}{2\mu} \frac{d^2}{dR^2} + \frac{l_n(l_n + 1)}{2\mu R^2} - (E - \Delta_n) \right] u_n(R) + \sum_{n'} \tilde{V}_{nn'}(R) u_{n'}(R) = \tilde{S}_{vj}^{(n)}(R) \quad (16)$$

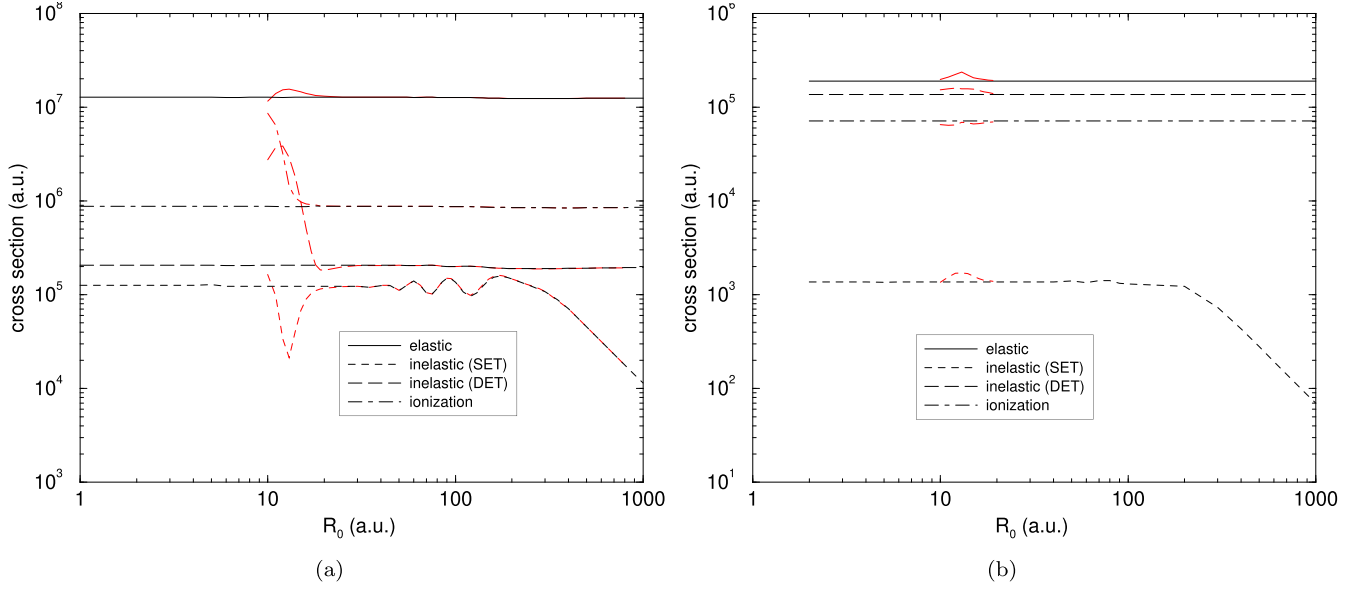


FIG. 2. Cross sections as a function of R_0 . Panel (a) is for collision energy of 10^{-10} a.u. The red curves show great sensitivity when R_0 goes below 20 a.u. due to the incompleteness of the atomic basis set in this region. The black curves show that the overlap inversion method (see text) is able to smooth out this sensitivity. Panel (b) shows a similar plot for collision energy of 10^{-6} a.u. The overlap inversion method is not as important at higher energies due to the centrifugal barrier, which prevents higher partial waves from entering the region where atomic basis set truncation errors would be problematic.

for the nuclear motion, where l_n is the orbital angular momentum for the n th channel, μ is the reduced mass, and

$$S_{vj}^{(n)}(R) = \chi_{vj}(R) \sum_m U_{nm}(R) \left[\frac{\Gamma_m(R)}{2\pi} \right]^{1/2} \quad (17)$$

is a source term that depends on the rovibrational wave function $\chi_{vj}(R)$ of the H_2^+ ($\bar{\text{H}}_2^-$) molecule and the widths for autoionization. Conservation of energy yields $E = \frac{k_e^2}{2} + \epsilon_{vj} - 6.8$ eV, where k_e is the electron (positron) momentum and ϵ_{vj} is the rovibrational energy. The fine-structure and Lamb shift contributions are included by adding the atomic energy defects Δ_n along the diagonal. These defects have been measured for antihydrogen by the ALPHA collaboration [26], where the fine-structure and Lamb shift splittings were found to be consistent with the hydrogenic values at the level of 2% and 11%, respectively. Energy defects for hydrogen were used in our calculations.

The sensitivity of the numerical results to the basis set truncation error was assessed by turning on the R dependence of $U_{ij}(R)$ at different distances R_0 . Figure 2(a) shows cross sections as a function of R_0 for a relative kinetic energy of $10^{-10} E_h$. As expected, the SET cross section falls to zero when R_0 is large due to the removal of R -dependent nonadiabatic coupling to the $(2s, 2p)$ state. All of the cross sections show strong variation at small R_0 when the diabatic coupling (11) is used due to the loss of unitarity associated with the truncated atomic basis set. The overlap inversion method described above is able to smooth out this sensitivity to yield cross sections that are virtually identical for all $R_0 < 20$ a.u. The ultracold limit provides the most stringent test of the overlap inversion method since there is no centrifugal barrier for s -wave scattering. At higher collision energies, such as $10^{-6} E_h$ shown in Fig. 2(b), the centrifugal barrier

prevents the system from entering the region where atomic basis set truncation errors would be problematic. It is clear that the sensitivity in the $R_0 < 20$ a.u. region is reduced compared to Fig. 2(a). The amplitude of the oscillations in the SET cross section around 100 a.u. is also reduced at higher collision energies. The numerical insensitivity to small R_0 agrees with previous studies [21] and suggests the error introduced by truncation of the atomic basis set may be mitigated with the overlap inversion method.

The spin-polarized atoms approach in the $^3\Sigma_u^+$ state. The emitted electron must have odd angular momentum and the transition obeys the selection rule $j = l \pm 1$ in order to preserve the overall ungerade symmetry of the system. The ionization cross sections are then given by

$$\sigma_{vj} = \frac{2\pi^3}{\mu E} [(j+1) | \langle u_{j+1}^{(n)} | \tilde{S}_{vj}^{(n)} \rangle |^2 + j | \langle u_{j-1}^{(n)} | \tilde{S}_{vj}^{(n)} \rangle |^2]. \quad (18)$$

Following [19], the H_2^+ Hamiltonian is diagonalized in a Sturmian (L^2) basis set to obtain both the bound-state (negative-energy) and pseudostate (positive-energy) wave functions. The associative and Penning ionization cross sections are then resolved using

$$\sigma_A = \sum_{j=0}^{j_{\max}} \sum_{v=0}^{n_j} \sigma_{vj}, \quad (19)$$

$$\sigma_P = \sum_{j=0}^{j_{\max}} \sum_{v=n_j+1}^{v_{\max}} \sigma_{vj}, \quad (20)$$

where n_j is the index of the last bound vibrational level for the rotational level j and the dissociative continuum is described by pseudostates with $v > n_j$.

The cross sections for SET, DET, and total ionization are computed within the CS approximation as in previous work [20,21] and are given by

$$\sigma_{\psi \rightarrow \psi'} = \frac{2\pi}{k_\psi^2} \sum_l (2l+1) |T_{\psi \rightarrow \psi'}^{(l)}|^2, \quad (21)$$

$$\sigma_{\psi \rightarrow \text{ion}} = \frac{2\pi}{k_\psi^2} \sum_l (2l+1) \left[1 - \sum_{\psi'} |S_{\psi \rightarrow \psi'}^{(l)}|^2 \right], \quad (22)$$

where sums are taken over even values of l due to proton symmetrization. Nonadiabatic angular coupling may be included using the total angular momentum $\vec{J} = \vec{j} + \vec{l}$. The corresponding cross sections are given by [21]

$$\begin{aligned} \sigma_{\psi \rightarrow \psi'} &= \frac{2\pi}{k_\psi^2} \sum_{JM} \sum_{J'M'} \sum_{lm} \sum_{l'm'} (2J+1)(2J'+1) \\ &\times [T(J)]_{l_a, l_b, j_a, j_b, j, l}^{l'_a, l'_b, j'_a, j'_b, j', l'} [T^*(J')]_{l'_a, l'_b, j'_a, j'_b, j', l'} \\ &\times \begin{pmatrix} j & l & J \\ \Omega & m & -M \end{pmatrix} \begin{pmatrix} j' & l' & J' \\ \Omega' & m' & -M' \end{pmatrix} \\ &\times \begin{pmatrix} j & l & J' \\ \Omega & m & -M' \end{pmatrix} \begin{pmatrix} j' & l' & J \\ \Omega' & m' & -M \end{pmatrix}, \quad (23) \end{aligned}$$

$$\begin{aligned} \sigma_{\psi \rightarrow \text{ion}} &= \frac{2\pi}{k_\psi^2} \sum_{JM} \sum_{l'l'} \begin{pmatrix} j & l & J \\ \Omega & M - \Omega & -M \end{pmatrix}^2 \\ &\times (2J+1) \{ 1 - |[S(J)]_{l_a, l_b, j_a, j_b, j, l}^{l'_a, l'_b, j'_a, j'_b, j', l'}|^2 \}. \quad (24) \end{aligned}$$

III. RESULTS

The set of inhomogeneous differential equations (16) and the associated set of homogenous equations are both solved using the renormalized Numerov method subject to appropriate boundary conditions [27]. For the source term, the bound rovibrational wave functions and the continuum pseudostates are obtained by diagonalization of the H_2^+ ($\bar{\text{H}}_2^-$) Hamiltonian in the orthonormal Laguerre polynomial basis set

$$\phi_{l,n}(R) = \sqrt{\frac{an!}{(n+2l+2)!}} (aR)^{l+1} \exp(-aR/2) L_n^{(2l+2)}(aR). \quad (25)$$

The nonlinear scale parameter a was varied to provide stationary PI cross sections [19]. AI cross sections are less sensitive to this parameter. The maximum vibrational level v_{max} was 100 for all energies and j_{max} ranged from 2 to 76, depending on the collision energy. When the source term is omitted, the coupled set of homogeneous equations, corresponding to the Schrödinger equation for a complex potential, allows total ionization cross sections to be calculated. It also allows computation of the elastic and inelastic (SET and DET) scattering cross sections. In all calculations, the sum of AI and PI cross sections, σ_A and σ_P , is compared with the total ionization cross section computed by solving the equations without the source term. Excellent agreement was found in all cases, which indicates that the basis set (25) is well converged. Calculations were also performed with and without the atomic energy defects in order to assess the impact of the additional couplings that become important at low collision energies.

Results with energy defects Δ_n set to zero are shown in Fig. 3. Panel (a) shows cross sections for AI and PI compared to power-law fits to high-energy data [19]. In contrast to the low-energy extrapolations obtained from the fitting formulas, and consequently the expectations of the previous study [13], we find that PI continues to dominate over AI as the energy is decreased. The fit $\sigma = 14.4E^{-2/3}$ was determined from the Langevin model, and it describes the total ionization cross section quite well over this energy range. It also describes the PI data, since PI is the dominant process. However, the fit to the AI data starts to deviate from calculated cross sections at the lower energies. This fit is based on the prefactor in Eq. (18). The deviation from the fit indicates that the transition matrix elements in Eq. (18) exhibit a greater energy dependence for lower collision energies.

Figure 3(b) compares cross sections that neglect spin with those that incorporate fine structure and Lamb shift. The cross sections exhibit greater energy dependence and more structure when spin is included. At low energies, SET is higher when spin effects are included, whereas DET is substantially reduced. It is interesting to note that the two sets of curves do not reach full agreement until $E > 10^{-3}$ a.u., whereas the fine-structure splittings are about 1000 times smaller than this collision energy. This sensitivity is due to the long range of the molecular potentials. The autoionization widths are much shorter in range, which allows better agreement in the ionization curves above $E > 10^{-6}$ a.u. This is consistent with the relatively short distance (~ 100 a.u.) required to match the boundary condition for the inhomogeneous problem, compared to the much longer distance ($\sim 10\,000$ a.u.) for the homogeneous case. Nevertheless, a small increase in ionization occurs for energies between 10^{-5} and 10^{-3} a.u. compared to the degenerate states approximation, which continues to follow the $O(E^{-2/3})$ behavior predicted by the Langevin model.

Figure 4 shows cross sections determined by including the fine-structure and Lamb shift energy defects in the set of coupled equations (16). Panel (a) shows AI and PI cross sections computed from the inhomogeneous set and compares their sum to the total ionization cross section computed from the homogenous set. As noted above, the agreement is very good over the whole range of collision energies. The high-energy fitting formulas are also shown. Not only is there no crossing point for the AI and PI curves at low energies, but a substantial reduction in the magnitude of both cross sections may be seen compared to the high-energy fits. This was taken into consideration in [13] by rescaling the relative AI and PI contributions obtained from the high energy fits to the total ionization cross sections [20] at the lower energies.

Figure 4(b) compares the total ionization cross section with the SET and DET cross sections. Also shown are the previous results [20], which were used to rescale the low-energy AI and PI cross sections [13]. The previous results, which neglected nonadiabatic radial coupling to the $(2s, 2p)$ state in the diabatic potential (11), show good agreement with the present DET and ionization results above 10^{-6} a.u., but the neglected coupling prevents SET transitions from occurring. At lower energies, significant differences may be seen in the present cross sections. The rescaling procedure used in [13], therefore, introduces some additional uncertainty due to the

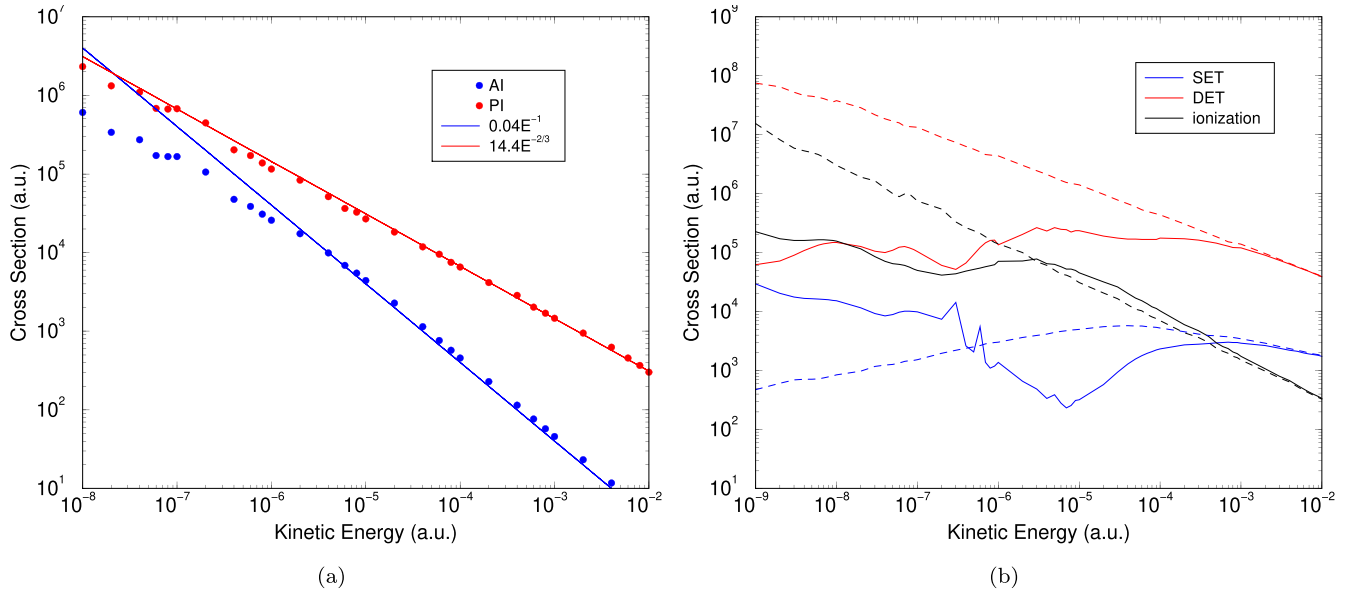


FIG. 3. Panel (a) shows cross sections for AI (blue points) and PI (red points) within the degenerate states approximation; these cross sections were computed by neglecting fine structure and the Lamb shift. Power law fits to the high-energy data from the previous study [19] are shown as solid lines. The AI cross sections deviate from the fit below 10^{-6} a.u., so there is no crossing of the actual data in contrast to the extrapolated curves. Panel (b) compares SET, DET, and total ionization cross sections for calculations that included fine structure and Lamb shift (solid curves) and calculations that used the degenerate states approximation (dashed curves).

missing coupling in the previous results [20]. Perhaps more importantly, the present DET cross sections show strong deviation from the previous results at low energies. In the range 10^{-8} – 10^{-7} a.u., the present DET curve is significantly higher than the previous result and continues to be the dominant energy transfer process. Below 10^{-8} a.u., the ionization cross section is largest as the DET curve falls below the previous

result. SET and DET are comparable as the ultracold Wigner threshold regime is reached at energies below 10^{-10} a.u..

Figure 5 shows rate coefficients for the various processes as a function of temperature. The DET and ionization rate coefficients have been multiplied by 2 to account for the loss of two metastable particles per collision. There is also a factor of 2 enhancement in the *s*-wave partial cross sections due

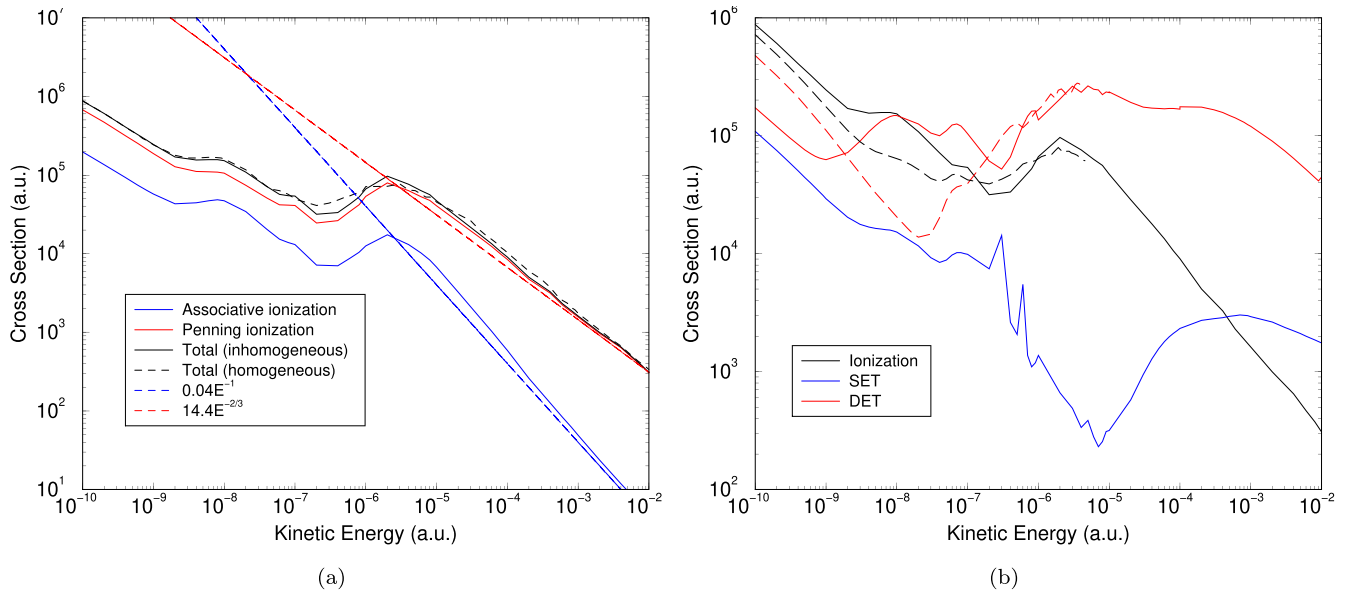


FIG. 4. Ionization cross sections as a function of kinetic energy. Panel (a) shows that the AI and PI cross sections are both substantially lower than the extrapolated curves obtained from the high-energy data [19]. The total ionization cross section, computed using homogeneous and inhomogeneous methods, shows very good agreement over the whole energy range. Panel (b) compares the total ionization cross section with inelastic SET and DET cross sections. The dashed curves are results [20] which neglected nonadiabatic radial coupling to the ($2s$, $2p$) state.

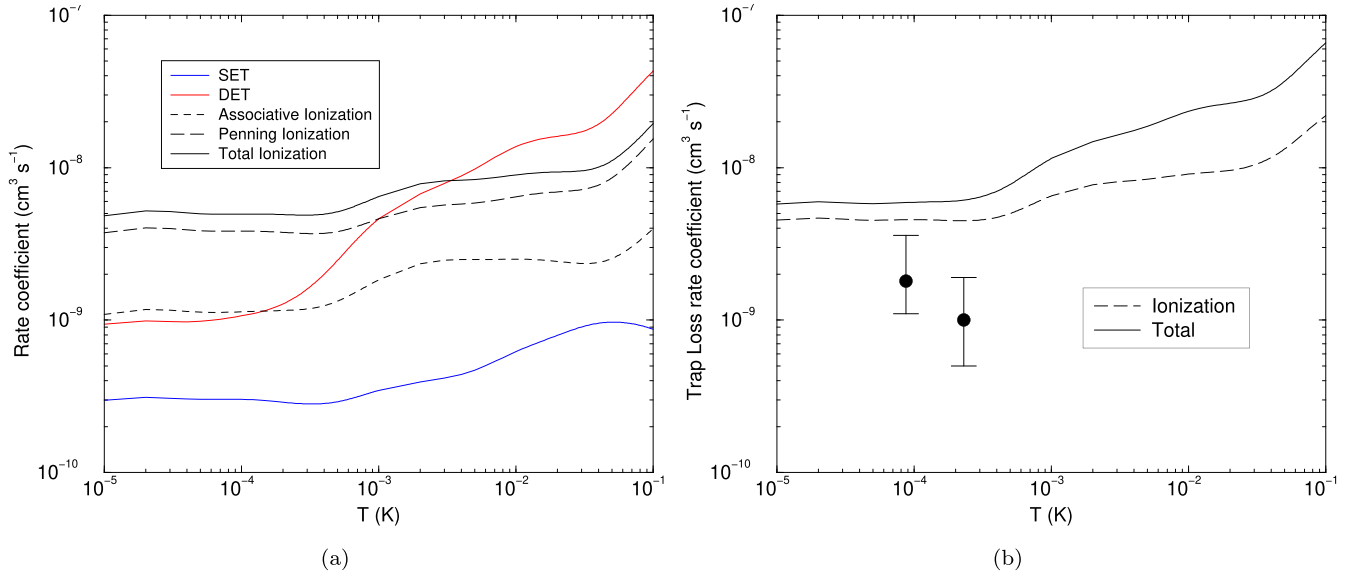


FIG. 5. Panel (a) shows rate coefficients as a function of temperature. The DET and ionization rates have been multiplied by 2 to account for the loss of two metastable particles per collision. Panel (b) shows trap loss rate coefficients compared to MIT experimental data [28]. The dashed curve is the total ionization rate coefficient (AI+PI) and the solid curve is the total trap loss rate coefficient (AI+PI+SET+DET).

to the identical nuclei. In other words, if the complex scattering length $a = \alpha - i\beta$ is defined for the entrance ($2s, 2s$) channel, with β representing inelastic losses including ionization, then the limiting zero-energy cross sections are given by $\sigma_{\text{el}} = 8\pi|a|^2$ and $\sigma_{\text{in}} = 8\pi\beta/k$, which are twice the respective values for distinguishable particle collisions [29].

Figure 5(b) compares the total rate coefficients with MIT trap loss data [28]. Similar to previous findings [19,30] at thermal energies, the theoretical results are larger than the experimental data and the agreement is improved if the theoretical rates are rescaled by a factor between 2 and 4. This discrepancy is likely due to limitations of the CS formulation, which often provides reliable estimates of relative transition probabilities even when there are errors in the absolute values. This is discussed in more detail below.

IV. DISCUSSION

As noted above, the largest source of uncertainty in the present CS calculations is the neglect of nonadiabatic angular couplings arising from the Coriolis interaction. Some effort has been made to address this issue. One approach [31,32] is to include the Coriolis coupling in the set of coupled equations and obtain the scattering matrix in the body-fixed frame. The transformation

$$|jl\rangle = (2l+1)^{1/2} \sum_{\Omega} \begin{pmatrix} j & l & J \\ \Omega & 0 & -\Omega \end{pmatrix} |j\Omega\rangle \quad (26)$$

back to the space-fixed frame is applied to ensure the channels have the correct asymptotic behavior for a given orbital angular momentum l . Unfortunately, the increase in the number of coupled equations and their slow fall-off, which requires propagation to extremely large distances, have so far rendered this approach to be impractical. An alternative approach [22] applies a molecular-to-atomic gauge transformation in a space-fixed frame to remove all nonadiabatic angular

couplings that arise from the vector potential in the separated atom limit. Short-range off-diagonal ($\Omega \leftrightarrow \Omega'$) elements induced by the vector potential are generally small and may be neglected [22]. The resulting transformed scalar potential

$$V_{n,n'}^{(JM)}(R) = [(2l+1)(2l'+1)]^{1/2} \times \sum_{\Omega} \begin{pmatrix} j & l & J \\ \Omega & 0 & -\Omega \end{pmatrix} \begin{pmatrix} j' & l' & J \\ \Omega & 0 & -\Omega \end{pmatrix} V_{n,n'}^{(J\Omega)}(R) \quad (27)$$

then allows the scattering matrix to be more efficiently computed in the space-fixed frame. The resulting cross sections are computed using Eqs. (23) and (24). This approach was attempted for the present system [21]. Unfortunately, the additional coupling and coordinate dependence of the unitary transformation (12), which connects the atomic and molecular basis sets, combined to make the gauge transformation (GT) approach more sensitive to basis set truncation error than was observed for the CS calculations. Nevertheless, useful insights may be gained from the GT method that allows an assessment of the importance of the neglected Coriolis terms in the CS results.

Figure 6 compares the CS and GT results. Panel (a) shows SET and DET rate coefficients computed with the GT method using different values of R_0 to turn on the R dependence of U_{ij} , similar to the procedure described above for the CS calculations. The GT curves are mostly insensitive to R_0 for temperatures above 30 mK as long as the value is not too large to exclude nonadiabatic radial coupling to the ($2s, 2p$) state. Below this temperature, the DET curves are uniformly lowered as R_0 is varied from 100 to 40 a.u. When R_0 is reduced further, the results (not shown) become more erratic due to atomic basis set truncation error. The ionization rates are much less sensitive to the choice of R_0 . Panel (b) compares GT and CS ionization rate coefficients. The shape of the curves

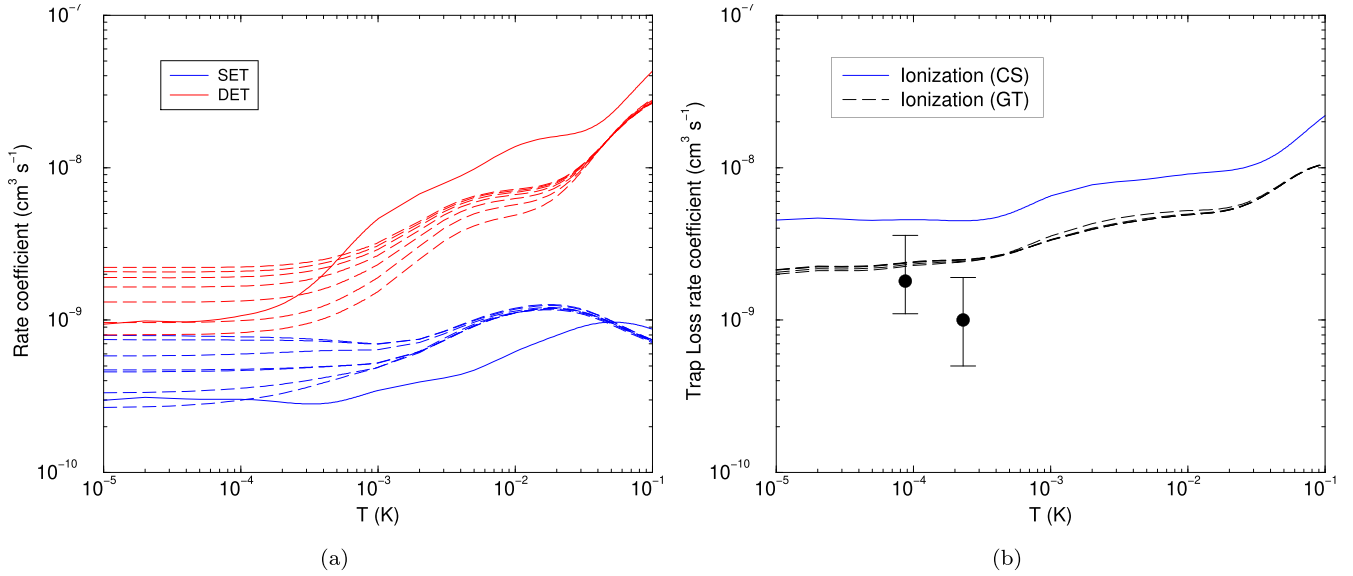


FIG. 6. Panel (a) shows SET (blue) and DET (red) rate coefficients computed with the GT method. The dashed curves used $R_0 = 40, 50, 60, 70, 80, 90, 100$ to compute the cross sections. Sensitivity appears for temperatures below 30 mK, where smaller DET rates are uniformly obtained as the value of R_0 is lowered. Also shown are the present CS results (solid curves). Panel (b) shows the GT ionization curves are much less sensitive for the same range of R_0 . The shape of the CS curve is very similar to the GT curve but approximately two times larger. The MIT trap loss data [28] are shown for comparison.

are very similar; however, the CS curve is larger by about a factor of 2. The GT results are in closer agreement with the MIT trap loss measurements [28]. This comparison neglects SET and DET contributions, which are presumably included in the experimental rate coefficients. Panel (a) shows the CS and GT calculations for these contributions have roughly the same behavior; however, there is no scaling factor that brings the curves into agreement, as in the ionization case. Therefore, it is not entirely clear which results should be recommended for the SET and DET rates. For ionization, it is clear that a factor of 2 rescaling of the CS results would bring the total ionization rate into better agreement with the MIT trap loss data [28] and the AI rate into better agreement with measurements at thermal energies [30]. It is also noteworthy that the downward trend shown in Fig. 6(a) for the DET curves with decreasing R_0 points to the possibility that DET may be a less significant source of trap loss than indicated by the CS results.

V. CONCLUSION

A recent study [13] suggested that it may be feasible to produce antihydrogen molecular ions in the future by laser exciting cold antihydrogen atoms held in a magnetic trap. The desired $\bar{\text{H}}_2^-$ would then form by AI, which may occur during collision of two metastable $\bar{\text{H}}(2s)$ atoms. The proposed experimental scheme relied on low-energy extrapolations of thermal rates, which predicted that AI would be the fastest exothermic process. The present study, however, reveals that AI is about 2.5 times less efficient than PI at the mK temperatures required by the experimental scheme. Additionally, it is found that AI dominates over SET but is generally less

efficient than DET, except at sub-mK temperatures where the DET rate drops sharply. Future efforts to produce $\bar{\text{H}}_2^-$ via the AI formation route will therefore need to carefully account for these trap loss mechanisms.

The relative ionization contributions (AI and PI) were resolved using an inhomogeneous CS formulation which yields a set of coupled equations in a rotating body-fixed frame but neglects the influence of the Coriolis force. The total ionization results were confirmed by solving the homogeneous set of CS equations. The influence of neglected nonadiabatic angular coupling induced by the Coriolis interaction was assessed by comparing to a separate calculation performed in an inertial space-fixed frame, which utilizes a gauge transformation to remove all nonadiabatic angular couplings in the separated atom limit. The resulting GT cross sections showed qualitative agreement with the CS cross sections but are more prone to basis set truncation error. The CS total ionization rate may be brought into good agreement with the GT result by dividing by 2. This rescaling approximately accounts for the neglected Coriolis coupling and brings the CS ionization results into better agreement with two existing experiments [28,30]. Future work should also include hyperfine splitting. Although hyperfine defects are very small ($\Delta \sim 10^{-8} E_h$), the present study showed the fine-structure and Lamb shift defects had a strong influence on the scattering dynamics at collision energies that were ~ 1000 times larger than the splittings.

ACKNOWLEDGMENT

This work was supported at Penn State by NSF Grant No. PHY-1806180.

- [1] M. H. Holzscheiter, M. Charlton, and M. M. Nieto, *Phys. Rep.* **402**, 1 (2004).
- [2] M. Ahmadi *et al.* (The ALPHA Collaboration), *Nat. Commun.* **8**, 681 (2017).
- [3] M. Charlton, S. Eriksson, and G. M. Shore, *Antihydrogen and Fundamental Physics*, SpringerBriefs in Physics (Springer, Cham, 2020), pp. 87–90.
- [4] M. Doser, *Prog. Part. Nucl. Phys.* **125**, 103964 (2022).
- [5] M. R. Schenkel, S. Alighanbari, and S. Schiller, *Nat. Phys.* **20**, 383 (2024).
- [6] R. Pohl, *Nature (London)* **578**, 369 (2020).
- [7] E. G. Myers, *Phys. Rev. A* **98**, 010101(R) (2018).
- [8] E. G. Myers, *Hyperfine Interact.* **239**, 43 (2018).
- [9] C. Amole *et al.* (The ALPHA Collaboration), *Nucl. Instrum. Methods Phys. Res. Sect. A* **735**, 319 (2014).
- [10] M. Ahmadi *et al.* (The ALPHA Collaboration), *Nature (London)* **557**, 71 (2018).
- [11] D. Galli and F. Palla, *Astron. Astrophys.* **335**, 403 (1998).
- [12] S. Lepp, P. C. Stancil, and A. Dalgarno, *J. Phys. B: At. Mol. Opt. Phys.* **35**, R57 (2002).
- [13] M. C. Zammit, M. Charlton, S. Jonsell, J. Colgan, J. S. Savage, D. V. Fursa, A. S. Kadyrov, I. Bray, R. C. Forrey, C. J. Fontes *et al.*, *Phys. Rev. A* **100**, 042709 (2019).
- [14] C. J. Baker *et al.* (The ALPHA Collaboration), *Nature (London)* **592**, 35 (2021).
- [15] Reference [7] estimates the availability of $\overline{\text{H}}^+$ at a rate of $\sim 10^{-3} \text{ s}^{-1}$, which would yield an average $\overline{\text{H}}_2$ production rate of $\sim 5 \times 10^{-6} \text{ s}^{-1}$ due to the competing reaction $\overline{\text{H}}^+ + \overline{p} \rightarrow \overline{\text{H}} + \overline{\text{H}}$, which is 180 times more efficient.
- [16] J. Hornquist, P. Hedvall, A. E. Orel, and A. Larson, *Phys. Rev. A* **108**, 052811 (2023).
- [17] C. O. Rasmussen, N. Madsen, and F. Robicheaux, *J. Phys. B: At. Mol. Opt. Phys.* **50**, 184002 (2017).
- [18] P. H. Donnan, M. C. Fujiwara, and F. Robicheaux, *J. Phys. B: At. Mol. Opt. Phys.* **46**, 025302 (2013).
- [19] A. Bohr, A. Blickle, S. Paolini, L. Ohlinger, and R. C. Forrey, *Phys. Rev. A* **85**, 042710 (2012).
- [20] R. C. Forrey, S. Jonsell, A. Saenz, P. Froelich, and A. Dalgarno, *Phys. Rev. A* **67**, 040701(R) (2003).
- [21] R. C. Forrey, A. Dalgarno, Y. V. Vanne, A. Saenz, and P. Froelich, *Phys. Rev. A* **76**, 052709 (2007).
- [22] B. Zygelman, A. Dalgarno, and R. D. Sharma, *Phys. Rev. A* **49**, 2587 (1994).
- [23] S. Jonsell, A. Saenz, P. Froelich, R. C. Forrey, R. Cote, and A. Dalgarno, *Phys. Rev. A* **65**, 042501 (2002).
- [24] Y. V. Vanne, A. Saenz, A. Dalgarno, R. C. Forrey, P. Froelich, and S. Jonsell, *Phys. Rev. A* **73**, 062706 (2006).
- [25] A. Yanacopoulos, G. Hadinger, and M. Aubert-Frecon, *J. Phys. B* **22**, 2427 (1989).
- [26] M. Ahmadi *et al.* (The ALPHA Collaboration), *Nature (London)* **578**, 375 (2020).
- [27] J. P. Leroy and R. Wallace, *J. Phys. Chem.* **89**, 1928 (1985).
- [28] D. Landhuis, L. Matos, S. C. Moss, J. K. Steinberger, K. Vant, L. Willmann, T. J. Greytak, and D. Kleppner, *Phys. Rev. A* **67**, 022718 (2003).
- [29] N. Balakrishnan, V. Kharchenko, R. C. Forrey, and A. Dalgarno, *Chem. Phys. Lett.* **280**, 1 (1997).
- [30] X. Urbain, A. Cornet, and J. Jureta, *J. Phys. B: At. Mol. Opt. Phys.* **25**, L189 (1992).
- [31] R. Pack, *J. Chem. Phys.* **60**, 633 (1974).
- [32] R. B. Walker and J. C. Light, *Chem. Phys.* **7**, 84 (1975).